Different approximations of shallow fluid flow over an obstacle

B. T. Nadiga and L. G. Margolin
Los Alamos National Laboratory, Los Alamos, New Mexico 87545

P. K. Smolarkiewicz
National Center for Atmospheric Research, Boulder, Colorado 80307

(Received 15 August 1995; accepted 17 April 1996)

Three different sets of shallow water equations, representing different levels of approximation are considered. The numerical solutions of these different equations for flow past bottom topography in several different flow regimes are compared. For several cases the full Euler solutions are computed as a reference, allowing the assessment of the relative accuracies of the different approximations. Further, the differences between the dispersive shallow water (DSW) solutions and those of the highly simplified, hyperbolic shallow water (SW) equations is studied as a guide to determining what level of approximation is required for a particular flow. First, the Green-Naghdi (GN) equations are derived as a vertically-integrated rational approximation of the Euler equations, and then the generalized Boussinesq (gB) equations are obtained under the further assumption of weak nonlinearity. A series of calculations, each assuming different values of a set of parameters—undisturbed upstream Froude number, and the height and width of the obstacle, are then presented and discussed. In almost all regions of the parameter space, the SW and DSW theories yield different results; it is only when the flows are entirely subcritical or entirely supercritical and when the obstacles are very wide compared to the depth of the fluid that the SW and DSW theories are in qualitative and quantitative agreement. It is also found that while the gB solutions are accurate only for small bottom topographies (less than 20% of the undisturbed fluid depth), the GN solutions are accurate for much larger topographies (up to 65% of the undisturbed fluid depth). The limitation of the gB approximation to small topographies is primarily due to the generation of large amplitude upstream propagating solitary waves at transcritical Froude numbers, and is consistent with previous analysis. The GN approximation, which makes no assumptions about the size of the nonlinearity, is thus verified to be a better system to use in cases where the bottom topographies are large or when the bottom topographies are moderate but the flow transcritical. [S1070-6631(96)01708-4]

I. INTRODUCTION

Shallow water equations provide useful reduced dimension descriptions of free surface flows in systems like the oceans and the atmosphere. In this paper we consider three different sets of shallow water equations, representing different levels of approximation. We compare the numerical solutions of these different equations for flow past bottom topography in several different flow regimes. In several cases we compute the full Euler solutions as a reference, allowing us to assess the relative accuracies of the different approximations. We also study the convergence of the results of the more accurate DSW theories to those of the highly simplified hyperbolic shallow water theory, as a guide to determining what level of approximation is required for a particular flow.

The usual shallow water (SW) equations, familiar to geophysicists, can be derived from the three-dimensional Euler equations by making the hydrostatic approximation, i.e., ignoring the vertical acceleration, and then averaging the equations across the thin dimension of the flow. This corresponds to the limit $\sigma \to 0$, where $\sigma\ (=D/\lambda)$ is the shallowness or dispersion parameter, the ratio of a representative average depth to the horizontal length scale of interest. Better reduced dimensional descriptions can be derived by considering the nonhydrostatic pressure contributions. These descriptions differ from the usual SW equations by the presence of higher-order dispersive terms whose origin lies in the vertical acceleration, and so are termed dispersive shallow water (DSW) theories. Since the dispersive terms have their origin in nonhydrostaticity, one might expect that their importance in geophysics is restricted to small scale flows. A recent article,[1] however, suggests that the higher-order dispersive terms may be important on global scales also, specifically in the context of long term climate simulations. Here the point is that even though the dispersive terms are small, as estimated by scale analysis, the integration time is long. Estimates in that article suggest that the solution trajectories for barotropic flow in the ocean, one based on the SW equations and the other on DSW equations, could diverge noticeably on time scales like 30 years.

The Green-Naghdi (GN) equations are a particular set of DSW equations. They were first derived for one horizontal dimension and flat bottom assuming irrotationality by Su and Gardner.[2] They were independently derived in a more general setting, based on assumptions about the form of the velocity in the thin (vertical) dimension for a flat bottom by Green, Laws, and Naghdi,[3] and generalized by Green and Naghdi[4] for a varying bottom. The same equations have subsequently been rederived by many others.[5–8] The GN equations have been used in the computation of steady wave solutions of permanent form (with no bottom topography),[7] study of tidal basins,[9] and the generation of upstream-

 1070-6631/96/8(8)/2066/12/$10.00

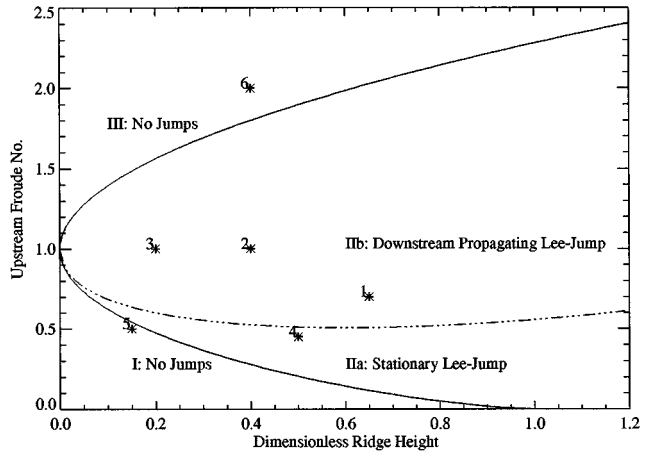

FIG. 1. The regime diagram for the hydrostatic shallow water equations. The x-axis is the dimensionless ridge height and the y-axis is the undisturbed Froude number. Region I is entirely subcritical, and the free surface dips symmetrically about the obstacle. Region III is entirely supercritical, and the free surface rises symmetrically about the obstacle. In region IIa, there is an upstream-propagating hydraulic jump and a stationary lee-side hydraulic jump. In region IIb, there is an upstream-propagating and a downstream-propagating hydraulic jump. The parameters corresponding to the six test cases presented in this article are also shown.

propagating solitary waves by moving disturbances in connection with ships moving in a channel.[10]

The Boussinesq equations[11] are an alternate DSW theory and date back to the 1870s. They assume both a flat bottom and a particular balance between the nonlinearity and the dispersion in the problem: $\delta=O(\sigma^2)$. Here $\delta(=A/D)$ is the nonlinearity parameter defined as the ratio of the typical amplitude of the deviation from equilibrium of the free surface to a representative depth. The Boussinesq equations have been generalized to include varying bottom topography and weak stratification (e.g., see Wu[12] and Camassa and Holm[13]). Different variations of generalized-Boussinesq (gB) equations have been used to study shallow fluid flow over topography (e.g., see Wu and Wu,[14] or Lee, Yates, and Wu[15]). In fact, the phenomenon of solitary waves propagating upstream of a moving surface pressure disturbance[16] was first numerically simulated using the gB equations.[14] A closely related set of equations that specialize to unidirectional waves, and which are valid when the flow is transcritical, are the forced Korteweg-de Vries (fKdV) equations. These equations have also been widely used to study the same phenomenon, but we do not address the fKdV equations in this paper since they are specialized to unidirectional waves, and are not valid over a wide range of Froude numbers. Neither do we consider extensions of the Boussinesq equations which use the velocity at a certain depth as a primary variable[17,18] or their nonlinear extensions,[19] since their primary utility seems to be in fluid layers of intermediate depths, where they have significantly improved dispersion properties.

In the flow over a two-dimensional ridge, discontinuities appear in the SW solutions both upstream and downstream of the ridge in the form of hydraulic jumps[20] (regions IIa and IIb of Fig. 1). If the shallowness parameter σ is identically zero, the higher-order dispersion terms in the DSW equations vanish and the usual SW equations are recovered. As shown later, for a nonzero value of σ, the DSW equations will resolve the discontinuities of the SW equations into trains of oscillations. In a physically analogous situation, but in the context of the simpler KdV equation, Lax, Levermore, and Venakides,[21] have proved the convergence of the (average over the oscillatory) KdV solution to the solution of the nondispersive equation in the limit of very small dispersion. Thus, though the DSW equations we study are nonlocal and have very different dynamical properties compared to the usual SW equations, we use the regime diagram of the SW equations, Fig. 1, as a guide to choosing the parameters we study.

Although the question of the importance of nonhydrostatic effects in long time climate simulations is of great importance, it is beyond the scope of this paper. Here we focus on three intermediate goals: first, we want to evaluate the utility of the GN approximation for accurately representing nonhydrostatic features of shallow fluid flow over a two-dimensional ridge by comparing with fully nonhydrostatic simulations of the Euler equations. (The geophysical counterpart of this flow would be a mesoscale atmospheric flow past a steep mountain or an oceanic flow past a seamount.) Second, considering the asymptotic dependence of the gB theory on the nonlinearity parameter, we want to establish the regions of validity of the gB equations as an adequate approximation of the nonhydrostatic flow. Finally, we would like to understand the convergence of the DSW descriptions to the SW description in the different regimes of Fig. 1.

The plan of our paper is as follows. To better illustrate the relationship between the SW, gB, and GN equations, we first present a derivation of these equations using the same approach. Thus, in section II we derive the GN equations as a vertically-integrated rational approximation of the Euler equations and show the further restriction (details in Appendix A) of the GN equations to the gB equations. In section III, we compare the GN and gB solutions against the fully nonhydrostatic Euler solutions for three different cases to assess the accuracies of the DSW theories. In section IV, we compare the SW solutions in the four different regimes of Fig. 1 against the corresponding DSW solutions, and in section V, we study the convergence of the GN solutions to the SW solutions in the limit of very wide topographical features. Conclusions are presented in section VI, and the numerical schemes are briefly described in Appendix B.

II. DERIVATION OF THE DSW EQUATIONS

A. The Euler equations

The behavior of the free surface of a homogeneous layer of fluid in the inviscid and incompressible limit is described by the Euler equations:

$$d_t\mathbf{u}+w\partial_z\mathbf{u}=-\frac{1}{\rho}\nabla p, \tag{1a}$$

$$d_t w+w\partial_z w=-\frac{1}{\rho}\partial_z p-g, \tag{1b}$$

where $\nabla=(\partial_x,\partial_y)$ is the two-dimensional horizontal gradient operator, $\mathbf{u}=(u,v)$ is the horizontal velocity field, w is the vertical velocity, and $d_t=\partial_t+\mathbf{u}\cdot\nabla$ is the horizontal two-dimensional material time derivative. In the system of coordinates used, z is in the direction of the vertical, $\mathbf{x}=(x,y)$ is in the horizontal, η is the depth of the fluid layer, b is the height of the bottom topography, and $b+\eta$ is the height of the free surface. These dynamical (prognostic) equations are supplemented by the constraint (diagnostic relation) of incompressibility expressed as the divergence free condition,

$$\nabla\cdot\mathbf{u}+\partial_z w=0. \tag{2}$$

The equality of the normal-velocity of the free-surface to the velocity of the fluid normal to the free-surface there gives rise to the kinematic boundary condition,

$$w=\partial_t(b+\eta)+\mathbf{u}(b+\eta)\cdot\nabla(b+\eta), \quad \text{at } z=(b+\eta)(\mathbf{x},t). \tag{3a}$$

Here we adopt the convention that if a term in round parentheses is preceded by a field and not an operator, then the field is evaluated at the location given by the term in the parentheses. The constancy of pressure at the free surface (at a prescribed value p_0) gives rise to the dynamical boundary condition

$$p(\mathbf{x},t)=p_0, \quad \text{at } z=(b+\eta)(\mathbf{x},t). \tag{3b}$$

The impermeability of the bottom surface gives rise to the bottom boundary condition,

$$w=\partial_t b+\mathbf{u}(b)\cdot\nabla b, \quad \text{at } z=b(\mathbf{x},t). \tag{4}$$

In particular flow situations, it is possible to define an average or representative depth D and a typical horizontal scale λ. There are then two parameters of interest: the shallowness or dispersion parameter σ defined as the ratio of the representative depth D to the typical horizontal scale λ, and the nonlinearity parameter δ defined as the ratio of typical amplitude A of a wave to the depth D. Since we are interested in a reduced-dimension description of shallow fluid systems, the shallowness parameter σ is a convenient small parameter for the analysis.

We nondimensionalize the various quantities as follows:

$$\mathbf{x}=\lambda\mathbf{x}^*, \quad z=Dz^*, \quad \eta=D\eta^*, \quad b=Db^*, \quad t=\frac{\lambda}{c_0}t^*, \quad \mathbf{u}=c_0\mathbf{u}^*, \quad w=\sigma c_0 w^*, \quad \text{and} \quad p=\rho_r c_0^2 p^*, \tag{5}$$

where $c_0=\sqrt{gD}$ is the long gravity wave speed corresponding to the depth D, and the nondimensionalization of w takes into account Eq. (2). Rewriting Eq. (1a), Eq. (1b) and Eq. (2) after dropping the asterisks, the nondimensional Euler equations are

$$d_t\mathbf{u}+w\partial_z\mathbf{u}=-\nabla p, \tag{6a}$$

$$\sigma^2(d_t w+w\partial_z w)=-\partial_z p-1, \tag{6b}$$

$$\nabla\cdot\mathbf{u}+\partial_z w=0. \tag{7}$$

Here $|\mathbf{u}|$ is the spatially and temporally varying Froude number based on the long gravity wave speed $\sqrt{gD}$. Note that this nondimensionalization does not assume the Froude number to be small; considering the importance of the small Froude number limit to oceanic flows, we will investigate this limit in a separate article.

B. The Green-Naghdi equations

As far as the continuity equation is concerned, no asymptotics are necessary and an integration of Eq. (7) from the bottom b to the free surface $b+\eta$ [along with the boundary conditions, Eq. (3a) and Eq. (4)] leads to

$$\overline{d_t}\eta=-\eta\nabla\cdot\overline{\mathbf{u}}, \tag{8}$$

where $\overline{d_t}=\partial_t+\overline{\mathbf{u}}\cdot\nabla$, and

$$\overline{\mathbf{u}}=\frac{1}{\eta}\int_b^{b+\eta}\mathbf{u}\,dz.$$

This is the exact vertically-averaged continuity equation, common to all vertically-averaged shallow water equations.

The form of the vertical momentum equation, Eq. (6b), gives us a rational basis to expand p in terms of σ^2 as

$$p(\mathbf{x},z,t)=p_0(\mathbf{x},z,t)+\sigma^2 p_1(\mathbf{x},z,t). \tag{9a}$$

Then from Eq. (6a), noting that $w=O(1)$ as a result of the nondimensionalization, we may expand $\mathbf{u}$ similarly as

$$\mathbf{u}(\mathbf{x},z,t)=\mathbf{u}_0(\mathbf{x},z,t)+\sigma^2\mathbf{u}_1(\mathbf{x},z,t). \tag{9b}$$

First we consider the part of the horizontal momentum equation, Eq. (6a),

$$d_t\mathbf{u}_0+w\partial_z\mathbf{u}_0=-\nabla p_0, \tag{10}$$

where $d_t=\partial_t+\mathbf{u}\cdot\nabla$. Note that this equation contains terms of different orders in σ^2. In an attempt to vertically integrate this equation, we proceed as follows. In the limit $\sigma\to 0$, the vertical momentum equation, Eq. (6b), yields

$$p_0(z)=b+\eta-z, \tag{11}$$

i.e., the pressure is hydrostatic. We assume the constant pressure at the free-surface, p_0 in Eq. (3b) equals zero in this paper. Further, if the initial conditions are such that $\partial_z\mathbf{u}_0=0$, then from Eq. (10) and Eq. (9b), $\partial_z\mathbf{u}_0=0$ for all times. In such a case, vertical integration of Eq. (10) from b to $b+\eta$ yields

$$\overline{d_t}\mathbf{u}_0=-\nabla(b+\eta). \tag{12}$$

Equations (8) and (12) (with $\overline{\mathbf{u}}=\mathbf{u}_0$), which constitute the leading-order approximation in the shallowness parameter ($\sigma\to 0$) are the classical shallow water equations.

Next we consider the remainder of the horizontal momentum equation: At $O(\sigma^2)$ we have

$$d_t\mathbf{u}_1+w\partial_z\mathbf{u}_1=-\nabla p_1. \tag{13}$$

Note that in any of the equations that appear at $O(\sigma^2)$, we can replace $\mathbf{u}$ by $\overline{\mathbf{u}}$ and d_t by $\overline{d_t}$ while incurring an overall error of only $O(\sigma^4)$. We vertically integrate Eq. (13) from b to $b+\eta$:

$$\int_b^{b+\eta} [\overline{d_t \mathbf{u}_1} + w\partial_z \mathbf{u}_1] dz$$

$$= \partial_t(\eta\overline{\mathbf{u}_1}) - \mathbf{u}_1(b+\eta)\partial_t(b+\eta) + \mathbf{u}_1(b)\partial_t b + \overline{\mathbf{u}}\cdot\nabla(\eta\overline{\mathbf{u}_1})$$
$$- \mathbf{u}_1(b+\eta)[\overline{\mathbf{u}}\cdot\nabla(b+\eta)] + \mathbf{u}_1(b)[\overline{\mathbf{u}}\cdot\nabla b]$$
$$+ [w\mathbf{u}_1]_b^{b+\eta} + \eta\overline{\mathbf{u}_1}(\nabla\cdot\overline{\mathbf{u}}) + O(\sigma^2)$$
$$= \eta\overline{d_t\mathbf{u}_1} + O(\sigma^2),$$

or

$$\eta\overline{d_t\mathbf{u}_1} = -\nabla(\eta\overline{p_1}) - p_1(b)\nabla b + O(\sigma^2). \tag{14}$$

To determine the nonhydrostatic pressure terms $p_1(b)$ and $\overline{p_1}$ in the above equation, we use the remainder of the vertical momentum equation, Eq. (6b), which at $O(\sigma^2)$ is

$$d_t w + w\partial_z w = -\partial_z p_1. \tag{15}$$

Since this equation is already at $O(\sigma^2)$, we can again replace $\mathbf{u}$ by $\overline{\mathbf{u}}$ and d_t by $\overline{d_t}$, incurring an overall effective error only of $O(\sigma^4)$. Vertically integrating the continuity equation, Eq. (7), from b to an arbitrary height z gives an expression for the vertical velocity w as

$$w(\mathbf{x},z,t) = \overline{d_t}b - (z-b)\nabla\cdot\overline{\mathbf{u}} + O(\sigma^2). \tag{16}$$

Then vertically integrating Eq. (15) from an arbitrary height z to the free-surface $b+\eta$, and making use of the boundary conditions Eq. (3b), Eq. (3a), and Eq. (4),

$$p_1(\mathbf{x},z,t) = \int_z^{b+\eta} [\overline{d_t}(\overline{d_t}b - (z-b)\nabla\cdot\overline{\mathbf{u}})$$
$$- (\overline{d_t}b - (z-b)\nabla\cdot\overline{\mathbf{u}})\nabla\cdot\overline{\mathbf{u}} + O(\sigma^2)]dz$$
$$= \int_z^{b+\eta} [\overline{d_t^2}b + (z-b)((\nabla\cdot\overline{\mathbf{u}})^2 - \overline{d_t}(\nabla\cdot\overline{\mathbf{u}}))$$
$$+ O(\sigma^2)]dz. \tag{17}$$

But from Eq. (8),

$$(\nabla\cdot\overline{\mathbf{u}})^2 - \overline{d_t}(\nabla\cdot\overline{\mathbf{u}}) = -\frac{1}{\eta}\overline{d_t}(\eta\nabla\cdot\overline{\mathbf{u}}), \tag{18}$$

and so

$$p_1(\mathbf{x},z,t) = (b+\eta-z)\overline{d_t^2}b - \frac{1}{2\eta}[\eta^2 - (z-b)^2]$$
$$\times\overline{d_t}(\eta\nabla\cdot\overline{\mathbf{u}}) + O(\sigma^2). \tag{19}$$

Therefore, the nonhydrostatic terms $p_1(b)$ and $\eta\overline{p_1}$ in Eq. (14) are

$$p_1(b) = \eta\overline{d_t}\left(\overline{d_t}b - \frac{1}{2}\eta\nabla\cdot\overline{\mathbf{u}}\right), \tag{20}$$

$$\eta\overline{p_1} = \eta^2\overline{d_t}\left(\frac{1}{2}\overline{d_t}b - \frac{1}{3}\eta\nabla\cdot\overline{\mathbf{u}}\right). \tag{21}$$

Adding σ^2 times Eq. (14) to Eq. (12), and rewriting in the dimensional form, we get

$$\overline{d_t\mathbf{u}} = -g\nabla(b+\eta) - \frac{1}{\eta}(\nabla(\eta\overline{p_1}) + p_1(b)\nabla b) + O(\sigma^4). \tag{22}$$

Here, $\eta\overline{p_1}$ and $p_1(b)$ are given by Eq. (21) and Eq. (20), respectively, but now in the dimensional variables. It is worth noting here that at the initial instant (and therefore at all later times), the horizontal velocity has been assumed to be z-independent at the leading order [$\mathbf{u}_0 = \mathbf{u}_0(\mathbf{x},t)$, but $\mathbf{u}_1 = \mathbf{u}_1(\mathbf{x},z,t)$ in Eq. (9b)]. The equations (22) and (8), resulting from such a near-columnar motion are called the level-I Green-Naghdi equations.

C. The generalized-Boussinesq equations

In deriving the GN equations (above), we made no assumptions about the nonlinearity parameter δ. To restrict the GN equations to the weakly nonlinear regime, we assume $\delta \ll 1$, i.e., the deviation from equilibrium of the free surface and the deviation of the flow velocity from the ambient are both small. In particular, we assume the Boussinesq balance $\delta = O(\sigma^2)$. To be consistent with this assumption that the response is small, we must assume that the bottom topography (forcing) is also small: $b = O(\delta)$. Since the dispersive terms in Eq. (22) are of higher order than the classical shallow water terms, we can linearize those dispersive terms (see Appendix A). The resulting momentum equations are

$$\overline{d_t\mathbf{u}} = -g\nabla(b+\eta) + \frac{\eta_0}{2}D_t(\nabla\nabla\cdot(\eta_0\overline{\mathbf{u}}))$$
$$- \frac{\eta_0^2}{6}D_t(\nabla\nabla\cdot\overline{\mathbf{u}}), \tag{23}$$

where η_0 is the undisturbed depth of the fluid layer (assuming a flat free surface), and while $d_t = \partial_t + \overline{\mathbf{u}}\cdot\nabla$ as before, we have now introduced the linear derivative $D_t = \partial_t + \mathbf{U}\cdot\nabla$, where $\mathbf{U}$ is the constant ambient flow velocity. These are the usual gB equations for variable bottom topography, presented here in a frame in which the topography is fixed—a frame natural for the problems in which we are interested.

III. COMPARISON OF THE DSW SOLUTIONS TO THE EULER SOLUTIONS

In this section we compare the GN and the gB solutions against the Euler solutions for three different cases. The simulated problem in each case is the flow over a two-dimensional ridge, with the different cases representing different choices of Froude number and the height of the ridge. In all the three cases, the ridge has the form

$$b(x) = b_c(1 + |x|^2/L^2)^{-1.5}, \tag{24}$$

with the half-width parameter L set to 1.0. The height of the ridge is changed by varying b_c.

Cases 1 and 2 are designed to challenge the GN theory. In case 1 the ridge height is a large fraction of the total layer thickness ($b_c = 0.65$). In case 2, the incoming velocity is critical (i.e., $F_u = 1.0$). Finally in case 3, the height of the ridge is reduced to 0.2 to make it closer to the range of validity of the assumptions going into deriving the gB approximation.

A. Case 1

We begin with the example of a ridge with dimensionless height $b_c = 0.65$ in a flow whose undisturbed (upstream) Froude number $F_u = 0.7$. The nondimensional amplitude of the first upstream-propagating solitary wave in the full Euler solution (see the description below) for this case at time 30 is ≈ 0.7. Since the nondimensional height of the ridge and the amplitude of the solitary wave is so large, one might expect poor predictions from a vertically-integrated theory. The comparisons detailed below, however, indicate that is not the case and that the GN equations are able to predict both the amplitude and the time of formation of the solitary waves reasonably well, reiterating the nonasymptotic nature of the GN theory in the nonlinearity parameter δ. (We note that the GN equations were derived in section II from an asymptotic expansion of the Euler equations in only the shallowness parameter σ, with no assumptions being made about the nonlinearity parameter δ.)

In the present two-layer Euler computation (see Appendix B 1), the density of the upper layer is one hundred times smaller than that of the bottom layer. For numerical reasons, we smooth the density transition between the layers [in the form of a hyperbolic tangent profile, Eq. (B5)]. The upper layer is initially twice as thick as the bottom layer and the top of the upper layer is a rigid lid. The second-order accurate numerical algorithm[22] is based on semi-Lagrangian nonoscillatory forward-in-time methods.[23,24] The restoring boundaries minimize reflection of waves generated within the computational domain and insure steady inflow. In the Euler computation we used a horizontal cell size Δx of 5/64 and a time step of 2/64. (All lengths in the computations are in units of representative water depth D and the time is in terms of $\sqrt{D/g}$.) Figure 2 shows a time sequence of results from the Euler simulation at times 10, 20, and 30. The plots contain three isopycnic contours at densities values 0.105, 0.505, and 0.905 times the density of the lower layer. [The density of the lower layer is used as the reference density ρ_r in the nondimensionalization; see Eq. (5).] In addition, the instantaneous velocity field is indicated by arrows. While the generation of a train of upstream-propagating solitary waves is clear, the high level of irregular activity downstream of the ridge may only be interpreted as indicative of physical wave breaking. We do not consider the Euler solutions in this downstream region in our comparisons, since after wave-breaking, viscous mechanisms are important. However, to address issues of implicit numerical viscosity of the Euler solver, the same problem was repeated with a spatially fourth-order accurate method—a method with lesser implicit viscosity.[23,24] While the upstream solutions were visually identical but for a slightly reduced spreading of the isopycnals in the case of the fourth-order scheme, we found differences only on small scales in the region of breakdown of the flow, downstream of the ridge. This indicates the relatively inviscid nature of the upstream solution and a dependence on implicit viscosity of only the small scale features of the solution in the region of breakdown of the flow (downstream of the ridge).

The GN and gB models are also based on forward-in-time methods and use semi-Lagrangian integrations along fluid trajectories (see Appendices B 2 and B 3). The dispersive terms introduce new issues in the numerical approximations. Although these terms can be shown to be small based on scale analysis, an explicit approximation is stable only under further severe restrictions of the computational timestep. We postpone a discussion of these issues to Appendix B. The problem configurations for the GN and gB models are exactly the same as the lower layer of the Euler computation. The calculations are now one-dimensional, and the top and bottom boundary conditions are part of the equations themselves.

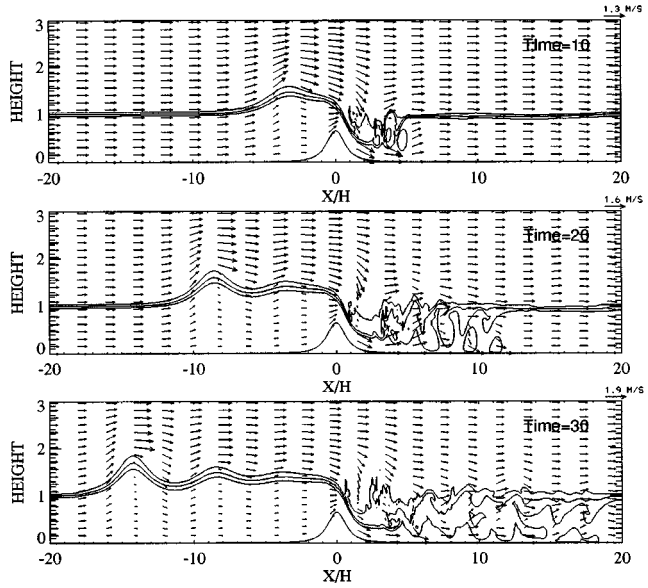

FIG. 2. $F_u = 0.7$ and $b_c = 0.65$. Snapshots of the Euler solutions at 10, 20, and 30 time units after the start of the flow. The ratio of the density of the lower layer to the upper layer is 100. The three iso-density contours are at 0.105, 0.505, and 0.905 times the density of the lower layer. The instantaneous velocity field is indicated by the arrows. All length scales are nondimensionalized by the undisturbed fluid depth in this and all the following figures.

In Fig. 3, we compare the 0.505 density contour from the Euler solution with the GN solution at the same three times. The continuous line is the GN solution and the heavy broken line is the Euler solution. The gB solution is also shown at the last time (time 30) in a lighter broken line for later reference. The GN solutions predict the amplitude of the train of upstream propagating solitary waves very closely (an error of less than 5%); however the GN solitary waves are generated slightly earlier than is predicted by the Euler equations. Based on our experience with this flow, we attribute this difference in part to the fact that the Euler equations use two layers of the fluid with a density ratio of a 100 (as mentioned previously), while the density ratio assumed in the GN theory is infinite. The GN equations fail to represent the flow correctly in the downstream side other than that they predict the correct minimum of the fluid surface behind the ridge. This is, however, only to be expected since the cnoidal waves that develop in the lee of the ridge cannot break in the GN computation, but do in the Euler equation computation. That is, by the very nature of the approximation, the break-

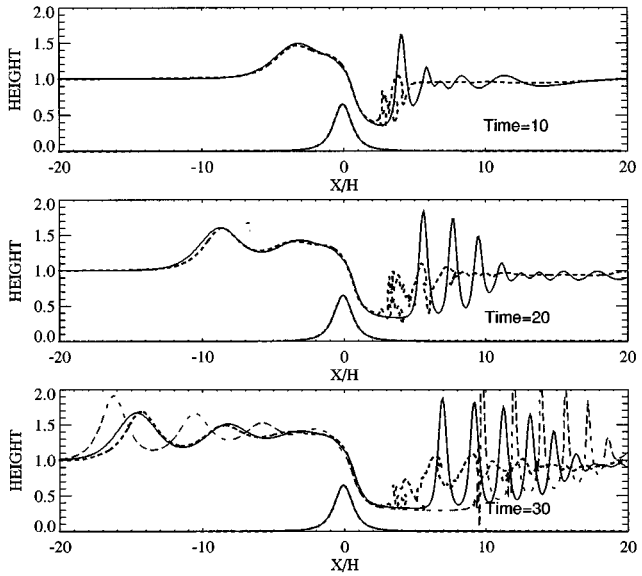

FIG. 3. $F_u = 0.7$ and $b_c = 0.65$. A comparison of the GN solutions at times 10, 20, and 30 with the 0.505 density contour of the Euler solutions. The heavy broken line is the Euler solution and the smooth continuous line the GN solution. At time 30, the gB solution is shown in a lighter broken line.

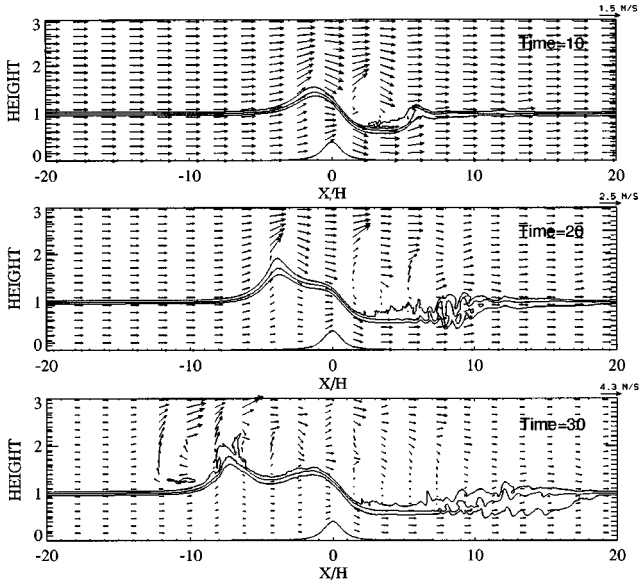

FIG. 4. $F_u = 1.0$ and $b_c = 0.4$. The Euler solutions at times 10, 20, and 30. The density ratio of the lower layer to the upper layer is 1000. The format of the picture is the same as in Fig. 2. Note the breaking of the first upstream-propagating solitary wave at time 30.

ing of waves is excluded in any of the reduced dimension shallow water descriptions. It remains to be verified whether the waves that develop in the GN calculation have the same wavelength as those that break in the Euler calculation.

Although a ridge height of 0.65 puts it far outside the range of validity of the gB approximation, we present the gB solution at time 30 in Fig. 3 (lighter broken line). The amplitude of the solitary waves is much larger and these waves are produced much earlier in the gB approximation. (The amplitude of the first solitary wave is in error by about 35%.) Also the depressed region on the downstream side has advanced much farther and there are some spurious oscillations near the first wave of the lee-side wavetrain. Despite these differences, it should be remarked that the gB approximation provides a fair prediction for this set of parameters, which lie outside the range of validity of the assumptions made in its derivation.

B. Case 2

In case 2, the flow is critical meaning that $F_u = 1.0$, and the ridge height b_c is chosen equal to 0.4. From the Euler solutions, we know that the first upstream-propagating solitary wave begins to break by time 30 for this choice of parameters and hence this case provides another severe test case for the GN equations.

The Euler simulation for case 2 is similar to that of case 1 excepting that the density ratio of the lower to the upper layer is set to 1000:1 as opposed to the 100:1 ratio used in the previous case. This larger value of the density ratio was chosen to test the sensitivity of the comparison between the Euler and the shallow water theories where the ratio is infinite. The larger density ratio in the Euler simulations does significantly reduce the small discrepancies between the speed and amplitude of the solitary waves in the two simulations noted in case 1. However the larger ratio also entails greater computational expense. In particular we had to set a tighter convergence level in the elliptic solver increasing the number of iterations, and also the timestep had to be reduced as the computation progressed.

Snapshots of the two-dimensional Euler computation are shown at times 10, 20, and 30 in Fig. 4. The format is the same as in Fig. 2, but now the three isopycnals are plotted for density values of 0.1005, 0.5005, and 0.9005 times the density of the lower layer. The breaking of the first upstream-propagating solitary wave is evident at time 30, and as before, the downstream waves have broken after time 10.

The comparison of the 0.5005 density contour of the Euler solutions with the GN solutions at times 10, 20, and 30 is shown in Fig. 5. In that figure, the jagged heavy broken lines are the Euler solutions, the smooth continuous lines are the GN solutions, and the gB solutions are plotted as lighter broken lines. The comparison between the Euler solutions and the GN solutions on the upstream side, i.e., the amplitude and speed of the upstream-propagating solitary waves and their time of formation is excellent up to time 30, when the Euler solution is beginning to show signs of breaking. As in the previous case, the height of the depressed region downstream of the ridge is very nearly the same in the Euler and GN solutions.

As in case 1, at a ridge height of 0.4 in case 2, the gB equations predict a larger amplitude of the upstream propagating solitary waves and an earlier time of formation. In this case, the amplitude of the first solitary wave is overpredicted by about 35%. There is better correspondence between the gB and GN solutions on the downstream side though the amplitudes of the gB waves are much larger. Interestingly, however, the shape of the Euler solitary wave seems closer to the gB representation than to the GN representation. In

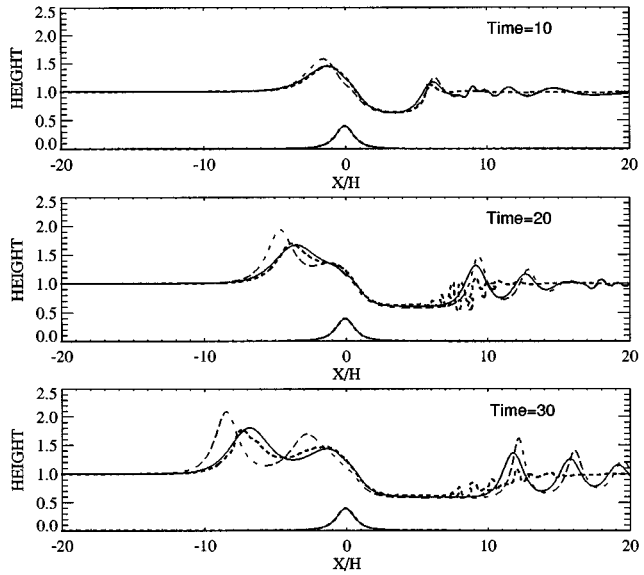

FIG. 5. $F_u=1.0$ and $b_c=0.4$. A comparison of the GN solutions at times 10, 20, and 30 with the 0.5005 density contour of the Euler solutions. The jagged heavy broken line is the Euler solution and the continuous smooth line is the GN solution. The gB solution is shown in lighter broken lines.

general, the GN solitary waves tend to be wider than the Euler solitary wave.

C. Case 3

In case 3, we choose the undisturbed Froude number as in case 2, $F_u=1.0$, but reduce the height of the ridge, b_c to 0.2 so that this case is closer to the range of validity of the gB approximation than is case 2. The mesh and timestep for both the GN and gB simulations are the same, and are identical to those used in cases 1 and 2. For the Euler run, we use a density ratio between the lower and upper layers of 1000:1, similar to case 2.

In Fig. 6, we compare the 0.5005 density contour from the Euler solutions (heavy broken jagged line) with the gB solutions (lighter smooth broken line) and the GN solution (smooth continuous line) for case 3. The snapshot is at time 40. We see that even at this small value of the ridge height the gB equations predict an earlier time of formation and a slightly greater amplitude for the upstream propagating solitary waves. The GN solutions again compare better in amplitude and time of formation of the solitary waves to the Euler solutions. The wider nature of the GN solitary waves (compared to the Euler solitary waves) is again evident.

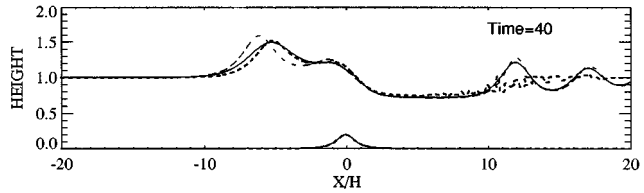

FIG. 6. $F_u=1.0$ and $b_c=0.20$. Snapshot at time 40 of the Euler (jagged heavy broken line), GN (continuous line), and gB (lighter broken line) solutions.

It is interesting to compare the downstream waves generated in the gB and GN simulations. The initial transient wave that moves downstream (not shown) is exactly the same in the two solutions. This agreement, as well as the close correspondence between the cnoidal waves far downstream (outside the window of presentation in this figure) is due to the fact that these are linear features of the DSW theories and are progressing over a flat bottom. We note that for the GN equations to go over to the gB equations, in addition to a linearization of the dispersive terms, it is necessary to make assumptions about the size of the bottom topography. A noticeable difference between the two solutions is the larger amplitude of the cnoidal waves just downstream of the depressed region of fluid behind the ridge and the slightly shorter wavelengths of these waves in the gB solutions.

The comparisons between the Euler solutions and the GN solutions in the above three cases demonstrate convincingly the utility of the GN equations for accurately predicting vertically-averaged features of a nonhydrostatic flow with large nonlinearities. Further, from the above test cases, we conclude that the gB theory is quantitatively adequate only when the bottom topographies are less than about 20% of the undisturbed water depth. This is in agreement with Lee, Yates, and Wu,[15] who found that the solutions of the gB equations agreed with tow-tank experiments for bottom topographies of about 15% of the undisturbed water depth.

IV. COMPARISON OF THE SW SOLUTIONS TO THE DSW SOLUTIONS

In the SW regime diagram of Fig. 1, there are four distinct regions: Region I where the flow is entirely subcritical, region III where the flow is entirely supercritical, and region II where there is an upstream-propagating hydraulic jump and a lee-side hydraulic jump. Region II is divided into two subregions: region IIa where the lee-side hydraulic jump is stationary and region IIb where the lee-side hydraulic jump propagates downstream. In this section we compare the SW solutions with the GN and gB solutions in each of these four regimes. As representative of region IIb, we consider case 2 discussed earlier, and for regions IIa, I, and III, we introduce cases 4, 5, and 6, respectively, where in case 4: $b_c=0.50$, $F_u=0.45$; case 5: $b_c=0.15$, $F_u=0.50$; case 6: $b_c=0.40$, $F_u=2.00$. The SW solutions (dot-dashed lines), the GN solutions (continuous lines), and the gB solutions (dashed lines) for these four cases are presented in Fig. 7.

As mentioned earlier, the SW theory differs from DSW theories by allowing the formation of discontinuities in the form of hydraulic jumps where the gradients of various quantities become infinite. After the formation of these hydraulic jumps, the solutions satisfy the SW equations only in a weak sense. In particular, the numerical model requires some dissipation of energy to regularize the solution and avoid unphysical oscillations. This dissipation usually takes the form of an artificial viscosity in numerical models, and is either implicit in the differencing scheme or is added explicitly. The second-order adaptive discrete-velocity method discussed in Nadiga,[25] provides one such implicit artificial viscosity scheme to simulate the SW equations. We have found

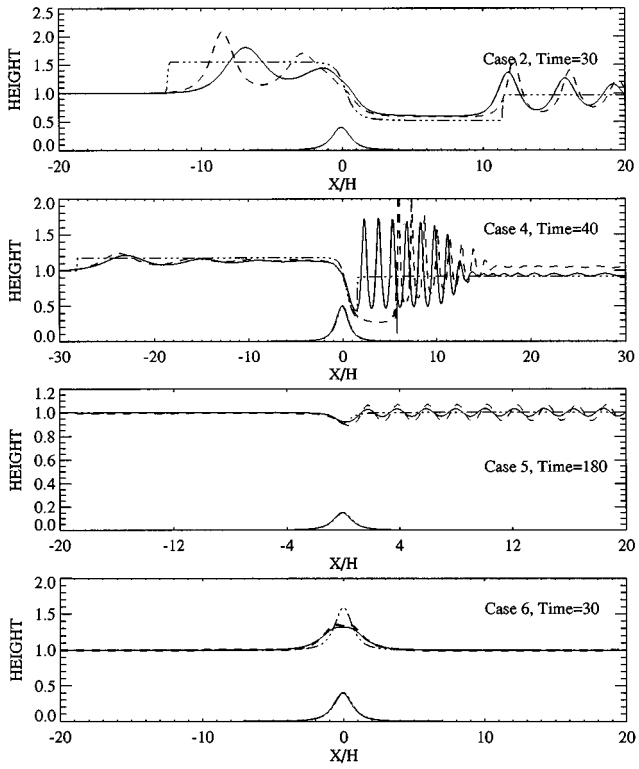

FIG. 7. A comparison of the SW solutions (dot-dashed lines), the GN solutions (continuous lines), and the gB solutions (dashed lines) for four cases corresponding to the four regions of Fig. 1. Case 2: $F_u=1.00$, $b_c=0.40$, time=30. Case 4: $F_u=0.45$, $b_c=0.50$, time=40. Case 5: $F_u=0.50$, $b_c=0.15$, time=180. Case 6: $F_u=2.00$, $b_c=0.40$, time=30. Note that the SW solutions overpredict the elevations and the depressions of the free surface.

this method superior to either adding explicit artificial viscosity to the semi-Lagrangian scheme or increasing the implicit viscosity by making the interpolation step of the semi-Lagrangian scheme nonoscillatory, i.e., the level of oscillation at a hydraulic jump is much smaller with the adaptive discrete-velocity method. The SW solutions for all the cases were computed using this adaptive discrete-velocity scheme. The same Δx of $5/64D$ (as in the previous Euler, GN, and gB computations) was used in the SW calculations and the time step corresponded to a CFL number of about 0.8. The errors in the SW solutions resulting from our numerical model, when compared to the asymptotically exact values for the SW equations, are of the order of 1%.

We consider a related aspect of the method of solution of the gB equations for case 4, the case where the SW equations develop a stationary lee side hydraulic jump (see Fig. 1). In this case, it was necessary to introduce a certain amount of artificial dissipation in the code for the gB solution while there was no such need for the GN solution. This dissipation resulted from making the interpolation step in the semi-Lagrangian solver nonoscillatory by adding donor cell flux corrections to the original centered differences. This was done on an *ad hoc* basis since there is no analytical theory to indicate that the introduction of an artificial dissipation would result in a weak solution of the gB equations. Further, the introduction of such dissipation affects the flow more globally than just in the region of steep gradients it was intended to resolve, and now the depressed region behind the ridge grows with time. (This is related to the nonlocal nature of the DSW theories.) The SW (i.e., $\sigma\rightarrow 0$) solution has a stationary hydraulic jump on the lee side of the ridge, and the GN solutions can be interpreted as having resolved this hydraulic jump into a train of waves, the leading edge of which stands at about the location of the hydraulic jump (see case 4 in Fig. 7). Such an interpretation is however, not possible with the gB solutions since the leading edge of the wave train is now propagating downstream. We are thus faced with a problem in the realization of the gB solutions, though perhaps only from a computational point of view—without the artificial dissipation, the calculation cannot be continued and with the dissipation, the $\sigma\rightarrow 0$ limit is lost.

The qualitative differences between the SW solutions and the DSW solutions (the GN and the gB solutions) for cases 2 and 4 (in Fig. 7) are attributable to the presence of discontinuities in the SW solutions. What is striking, however, is the trend of the SW equations in region IIb of Fig. 1 (represented here by case 2, Fig. 7) to predict a lower level of the free surface in the depressed region just downstream of the ridge and a higher level (compared to the average elevation of the DSW solutions) in the region upstream of the ridge. Considering only the region of the uniform depressed shelf downstream of the ridge in case 2, the SW solution is in error by at least 20%, noting that the GN solution for this case has been verified previously by direct comparison to the full Euler solution. This difference between the GN solution and the SW solution is at first sight disturbing. Since this region is locally flat, it would seem that the contributions of the dispersive terms would have to be negligible here, implying that the GN equations would have to predict the same depression of the free surface as the SW equations. The above argument is however incorrect in view of the fact that the DSW theories are nonlocal. A similar trend of overprediction of the elevation of the free surface upstream of the ridge and the depression of the free surface downstream of the ridge is evident in case 4 (in Fig. 7) also. Finally for cases 5 and 6 (see those cases in Fig. 7), though there are no discontinuities in the SW solutions, it is clear that there are still large dispersive corrections to the SW solutions. In fact, the SW solution in case 5 is qualitatively different from the DSW solution for that case downstream of the ridge. For cases 5 and 6, the differences between the GN and the gB solutions are of the same nature as discussed earlier.

The above comparisons between the SW solutions and the DSW solutions indicate that when the undisturbed upstream Froude number and the height of the bottom topography are such that discontinuities occur in the SW solutions, they are regularized by dispersion in the DSW solutions. While it is difficult to quantify this difference between the SW and DSW solutions, it is clear that the nonlocal nature of the DSW equations results in substantial quantitative corrections to the SW solutions even in uniform regions like the depressed shelf downstream of the obstacle.

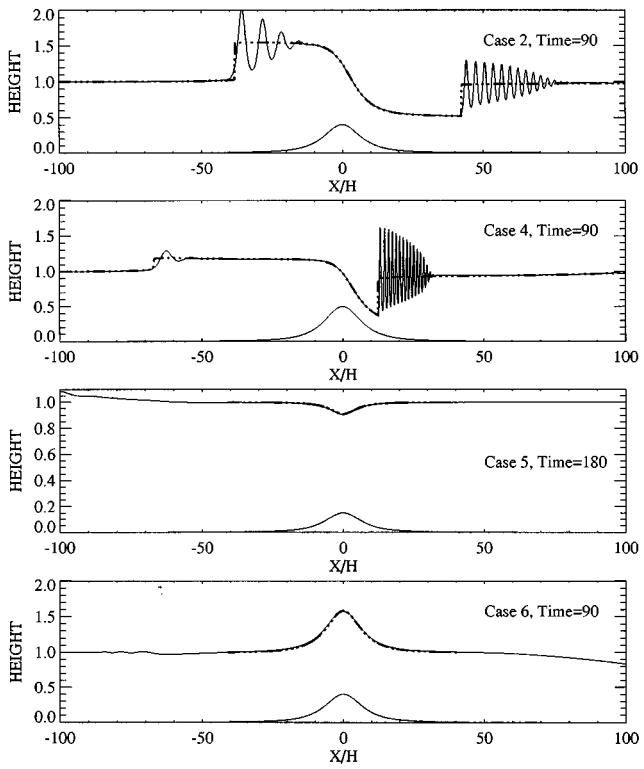

FIG. 8. The SW solutions (dot-dashed lines) and the GN solutions (continuous lines) for the same four cases as in Fig. 7. The only difference is that the ridges are now 10 times wider than in Fig. 7. The dispersive corrections are now confined to cases for which the SW solutions have discontinuities.

V. THE DISPERSIVE DIFFERENCES FOR VERY GENTLE TOPOGRAPHIES

In Fig. 8, we present the SW solutions (dot-dashed lines) and the GN solutions (continuous lines) for the same four cases as in Fig. 7, but now with the ridge in each of the cases being 10 times wider than in Fig. 7. The agreement between the SW solutions and the GN solutions is almost perfect for cases 5 and 6, and it is clear from cases 2 and 4 that for these very gentle bottom topographies, the differences between the SW solutions and the DSW solutions are mainly related to the discontinuities in the SW solutions.

In view of the above comparison between the SW solutions and the GN solutions, we may conclude that the SW level of description is a faithful representation of the flow only when the Froude number and ridge heights are such that the flow is either entirely subcritical or entirely supercritical and the slope of the ridge is very gentle. Our numerical results further suggest that in cases where the discontinuities of the SW solutions are regularized by dispersion in the DSW solutions, the DSW solutions converge in a weak sense (i.e., the average over the oscillations) to the SW solutions in the limit of extremely wide topographical features.

VI. CONCLUSIONS

Reduced dimension descriptions of inviscid shallow fluid flows are easier to simulate than the full three-dimensional Euler equations. Such descriptions have been derived at several different levels of approximation. The usual shallow water (SW) equations constitute the leading-order reduced dimension approximation derived from an asymptotic expansion in the shallowness parameter and assume hydrostatic balance. Nonhydrostatic terms at the next order restore the dispersive nature of the gravity waves and thus lead to dispersive shallow water (DSW) models. Since these model equations are obtained by a vertical-averaging procedure, wave breaking and related phenomena cannot be incorporated within this framework.

In this paper we first compared the relative accuracies of two DSW theories—the Green-Naghdi (GN) theory and the generalized Boussinesq (gB) theory—by making direct comparisons to the full Euler solutions in three different cases and then considered the relationship between the SW and DSW theories using three additional representative cases. Each set of equations were integrated numerically to solve the flow over a two-dimensional ridge. The DSW equations are a singular perturbation extension of the SW equations, and so required novel algorithmic formulations (discussed in Appendix B).

We find that the GN equations predict important features of the flow (excluding wave breaking) accurately over a wide range of parameters. The gB equations capture qualitatively the same features of the flow in all the regimes considered, although some of the cases were far outside of their asymptotic range of validity. For the gB model to be quantitatively correct, features of the bottom topography have to be less than about 20% of the undisturbed fluid depth. For most of the cases considered, the SW solutions were qualitatively incorrect. However this does not contradict the usefulness of the SW approximations for many applications. The appearance of the dispersive corrections to the SW equations as the highest-order derivatives leads to difficulties in quantifying the differences between the SW and DSW descriptions, but our numerical simulations seem to indicate that the DSW solutions converge in a weak sense (i.e., averaging over the oscillations) to the SW solutions in the limit of very wide topographical features.

ACKNOWLEDGMENTS

We are grateful to Darryl Holm and Roberto Camassa for valuable discussions on shallow water theory, and to Joseph Klemp, Richard Rotunno, William Skamarock, and an anonymous referee for useful comments on an earlier version of the manuscript. We would like to thank the Advanced Computing Laboratory at LANL and the MMM section at NCAR for making available their computing resources. This work has been supported in part by the U.S. Department of Energy CHAMMP program as part of the U.S. Global Change Research Program.

APPENDIX A: LINEARIZATION OF THE DISPERSIVE TERMS

Since no assumptions are made about the size of the nonlinearity in the derivation of the Green-Naghdi equations, the resulting dispersive terms there are nonlinear. In this appendix, we show how a linearization of the dispersive terms leads to the dispersive terms of generalized-Boussinesq

equations. For simplicity, considering stationary bottom topographies, the dispersion terms in the GN equations are

$$\frac{1}{\eta_*}\nabla\left[\eta_*^2 d_t\left(\frac{1}{3}\,\eta_*\nabla\cdot\mathbf{u}_* - \frac{1}{2}\,\mathbf{u}_*\cdot\nabla b_*\right)\right] + d_t\left(\frac{1}{2}\,\eta_*\nabla\cdot\mathbf{u}_* - \mathbf{u}_*\cdot\nabla b_*\right)\nabla b_*, \tag{A1}$$

where $b_*=b/D$, $\eta_*=\eta/D$, and $\mathbf{u}_*=\mathbf{u}/c_0$, i.e., no assumptions have been made on their sizes. If the nonlinearity is assumed small, i.e., the deviations from the ambient conditions are of order $\delta\ll 1$, then

$$\eta_*=\eta_0+O(\delta),\quad \mathbf{u}_*=\mathbf{U}+O(\delta)\Rightarrow\nabla\cdot\mathbf{u}_*=O(\delta),$$
$$b_*=O(\delta). \tag{A2}$$

In the above equation, $\mathbf{U}$ is the constant ambient velocity and $\eta_0=1-b_*$ is the depth of the undisturbed fluid layer. The latter also implies that $\nabla\eta_0=O(\delta)$. Further, since $d_t=\partial/\partial t+\mathbf{u}_*\cdot\nabla$, $d_t=D_t+O(\delta)$, where D_t is the linear derivative $\partial/\partial t+\mathbf{U}\cdot\nabla$. Inserting Eq. (A2) in Eq. (A1), we have

$$\frac{1}{\eta_0}\nabla\left[\eta_0^2 D_t\left(\frac{1}{3}\,\eta_0\nabla\cdot\mathbf{u}+\frac{1}{2}\,\mathbf{u}\cdot\nabla\eta_0\right)\right]+O(\delta^2). \tag{A3}$$

Note in the above equation that the second term of Eq. (A1) makes no contribution at the leading order in δ, and that there are still $O(\delta^2)$ terms in the first term of Eq. (A3). Further manipulation of Eq. (A3) under the same assumptions gives the linearized dispersion terms as

$$\frac{\eta_0}{2}\,D_t(\nabla\nabla\cdot(\eta_0\mathbf{u}))-\frac{\eta_0^2}{6}\,D_t(\nabla\nabla\cdot\mathbf{u}). \tag{A4}$$

APPENDIX B: THE COMPUTATIONAL MODELS

1. Numerical model for the Euler equations

We solve the incompressible Euler equations:

$$\frac{d\mathbf{v}}{dt}=-\frac{1}{\rho}\,\nabla\phi-g\left(1-\frac{\rho_0}{\rho}\right)\nabla z, \tag{B1a}$$

$$\frac{d\rho}{dt}=0, \tag{B1b}$$

$$\nabla\cdot\mathbf{v}=0, \tag{B1c}$$

where ϕ denotes the pressure perturbation from a hydrostatically balanced environment characterized by a density profile $\rho_0=\rho_0(z)$, g is the acceleration of gravity, and other variables have their usual meaning. Equations (B1) (cast in standard, nonorthogonal, terrain-following coordinates[26]) are integrated along flow trajectories on a discrete, regular, nonstaggered mesh using a second-order accurate semi-Lagrangian finite difference approximation of Smolarkiewicz and Pudykiewicz.[23] Briefly, the model algorithm treats the prognostic equations (B1a) and (B1b) in the symbolic form

$$\frac{d\psi}{dt}=F^{\psi}, \tag{B2}$$

whose integral along a parcel trajectory assumes the trapezoidal-rule approximation,

$$\psi_{\mathbf{i}}^{n+1}=(\psi+0.5\Delta t F^{\psi})_{\mathbf{o}}+0.5\Delta t F^{\psi}|_{\mathbf{i}}^{n+1}$$
$$\equiv\widetilde{\psi}_{\mathbf{o}}+0.5\Delta t F^{\psi}|_{\mathbf{i}}^{n+1}. \tag{B3}$$

Here n, $\mathbf{i}$, and Δt have the traditional meanings of the time level, position on the grid, and the temporal increment, respectively. The subscript $\mathbf{o}$ appearing at the first term on the right hand side of Eq. (B3) refers to a $\widetilde{\psi}$ field value at the departure point $(\mathbf{x}_{\mathbf{o}},t^n)$ of the trajectory arriving at the grid point $(\mathbf{x}_{\mathbf{i}},t^{n+1})$; here, it denotes an elaborate, second-order accurate, monotone, nonlinear interpolation algorithm.[24] The departure points $\mathbf{x}_{\mathbf{0}}$ are evaluated to second-order accuracy by a two pass iteration of

$$\mathbf{x}_{\mathbf{o}}=\mathbf{x}_{\mathbf{i}}+\int_{t^{n+1}}^{t^n}\mathbf{v}(\mathbf{x},t)\,dt,$$

approximated in the spirit of Adams-Bashforth schemes as

$$\mathbf{x}_{\mathbf{o}}=\mathbf{x}_{\mathbf{i}}-0.5\Delta t(\mathbf{v}_{\mathbf{o}}+2\mathbf{v}_{\mathbf{i}}^n-\mathbf{v}_{\mathbf{i}}^{n-1}), \tag{B4}$$

following the mid-point algorithm in section 4 of Smolarkiewicz and Pudykiewicz.[23] The elliptic pressure equation, which follows from the incompressibility constraint (B1c) imposed on the discretized momentum equation (B1a), is solved using the method of conjugate residuals (e.g., see Smolarkiewicz and Margolin[22,27] for algorithmic details and a further discussion).

The model setups adopted for the simulations in section III are as follows. The ambient conditions assume the uniform ambient flow of u_∞ and a density profile,

$$\frac{\rho_0(z)}{\rho_r}=\left(1-0.5\Delta\rho\left(1+\tanh\left(\frac{(z-D)}{\epsilon}\right)\right)\right), \tag{B5}$$

with $\Delta\rho$ either equal to 0.99 or 0.999, $D=1$, and $\epsilon=2/64$. The bell-shaped hill (24) forms the lower boundary of the model. The boundary conditions assumed are free-slip rigid-lid at both the top and bottom boundaries. At the lateral boundaries $u=u_\infty$; the gravity-wave absorbers near the lateral boundaries attenuate the solution toward ambient conditions with an inverse time scale that increases linearly from zero at the distance $26\Delta X\approx 2D$ from the boundary to $(16\Delta t)^{-1}\approx(3L/u_\infty)^{-1}$ at the boundary. The model domain $(x,z)\in[-20D,20D]\times[0,3D]$ is resolved with $NX\times NZ=512\times 96$ uniform grid increments $\Delta X=5/64$ and $\Delta Z=2/64$. The initial condition is the potential flow past the hill in Eq. (24). Details of the model performance in a similar flow situation may be found in Rotunno and Smolarkiewicz.[28]

2. Numerical model for the Green-Naghdi equations

The presence of high-order time derivatives on the right hand side of the Green-Naghdi equations written in a Lagrangian form complicates the semi-Lagrangian approximation of these equations. In the model that is used in the simulations of section III, the depth equation is solved explicitly to obtain the new depth and then the momentum equations are solved implicitly to obtain the new velocity fields. The departure point is found to second-order accuracy as in Eq. (B4), but now with the three-dimensional velocity field $\mathbf{v}$ replaced by the two-dimensional horizontal velocity field $\mathbf{u}$.

In what follows, we briefly present the modeling of the depth equation and the momentum equations separately.

A. The depth equation

With a provision for the restoring boundaries, the depth equation, Eq. (8), is now

$$\frac{d\eta}{dt} = -\eta\nabla\cdot\mathbf{u} - \frac{\eta-\eta_a}{\tau}. \tag{B6}$$

The instantaneous flow Jacobian J measures the rate of contraction or expansion of a parcel of fluid:[29]

$$J = \frac{\partial \mathbf{x}}{\partial \mathbf{x}_o} = \frac{\partial(x,y)}{\partial(x_o,y_o)}, \tag{B7}$$

and is evaluated following the departure point calculations of Eq. (B4). From the definition of the velocity divergence,[30]

$$\nabla\cdot\mathbf{u} = \nabla\cdot\frac{d\mathbf{x}}{dt} = \frac{1}{J}\frac{dJ}{dt}. \tag{B8}$$

Substituting Eq. (B8) in Eq. (B6),

$$\frac{1}{J}\frac{d\eta J}{dt} = -\frac{\eta-\eta_a}{\tau}. \tag{B9}$$

A mid-point integration (trapezoidal rule) over the parcel trajectory T connecting $(\mathbf{x}_0,t_0)$ and $(\mathbf{x}_i,t_1)$ results in

$$\frac{\eta J-\eta_o}{\Delta t} = -\frac{1}{2}\left\{\left[\frac{\eta-\eta_a}{\tau}\right]_0 + \frac{\eta-\eta_a}{\tau}J\right\}, \tag{B10}$$

where the Jacobian is calculated such that at the departure point J_0 is identically unity. Further manipulation of the above equation leads to an explicit expression for the depth of the fluid layer at the arrival grid point at the new time level:

$$\eta = \left[\eta - \frac{\Delta t}{2\tau}(\eta-\eta_a)\right]_0 J^{-1} - \frac{\Delta t}{2\tau}(\eta-\eta_a), \tag{B11}$$

rewritten for convenience as

$$\eta = \frac{\tilde{\eta}J^{-1} + \eta_a(\Delta t/2\tau)}{1+(\Delta t/2\tau)}. \tag{B12}$$

B. The momentum equation

With the boundary restoring terms included, the momentum equation is

$$\frac{d\mathbf{u}}{dt} = -\nabla(\eta+b) + \frac{1}{\eta}\nabla\left(\eta^2\frac{d\alpha}{dt}\right) + \frac{d\beta}{dt}\nabla b - \frac{\mathbf{u}-\mathbf{u}_a}{\tau}, \tag{B13}$$

where

$$\alpha = \left(\frac{1}{3}\eta\nabla\cdot\mathbf{u} - \frac{1}{2}\mathbf{u}\cdot\nabla b\right),$$

$$\beta = \left(\frac{1}{2}\eta\nabla\cdot\mathbf{u} - \mathbf{u}\cdot\nabla b\right),$$

from Eq. (22). Note that although at this stage η is known, the right hand side is nonlinear in $\mathbf{u}$. The dispersive terms in the above equation being the highest-order time derivatives in the equation necessitate an implicit solution of the two-dimensional velocity field. Manipulating the above equation to put it in a form more amenable to the semi-Lagrangian technique,

$$\frac{d\mathbf{u}}{dt} = -\nabla(\eta+b) + 2\frac{d\alpha}{dt}\nabla\eta + \eta\frac{d}{dt}\nabla\alpha + \eta\nabla\mathbf{u}\cdot\nabla\alpha + \frac{d\beta}{dt}\nabla b - \frac{\mathbf{u}-\mathbf{u}_a}{\tau}.$$

All the terms in the above equation can be evaluated at the mid-point of the Lagrangian trajectory (connecting the grid point at the advanced time level and the departure point at the known time level), except the $-\eta\nabla\mathbf{u}\cdot\nabla\alpha$ term. This term, which is quadratic in the $\nabla\mathbf{u}$, is much smaller than the other three dispersive terms and is evaluated entirely at the departure point without significantly affecting the overall accuracy of the integration. (This has been verified by using a predictor-corrector algorithm to evaluate the nonlinear term at the mid-point of the parcel trajectory.) Now writing down the mid-point integration formula for the above equation over the particle trajectory T results in

$$\begin{aligned}\frac{\mathbf{u}-\mathbf{u}_o}{\Delta t} = &-\frac{1}{2}(\nabla(b+\eta)+[\nabla(b+\eta)]_o) + (\nabla\eta+[\nabla\eta]_o)\\ &\times\frac{\alpha-\alpha_o}{\Delta t} + \frac{1}{2}(\nabla b+[\nabla b]_o)\frac{\beta-\beta_o}{\Delta t}\\ &+\frac{1}{2}(\eta+\eta_o)\frac{\nabla\alpha-[\nabla\alpha]_o}{\Delta t} + [\eta\nabla\mathbf{u}\cdot\nabla\alpha]_o\\ &-\frac{1}{2}\left(\frac{\mathbf{u}-\mathbf{u}_a}{\tau} - \left[\frac{\mathbf{u}-\mathbf{u}_a}{\tau}\right]_o\right),\end{aligned} \tag{B14}$$

where Q_0 indicates that the field Q is evaluated at the departure point $\mathbf{x}_0$. Since this equation is linear in $\mathbf{u}$, it may be symbolically written as

$$\mathscr{L}(\mathbf{u}) = \hat{\mathbf{u}},$$

where $\mathscr{L}$ is the linear operator in Eq. (B14). The complexity of the linear operator and the fact that the field to be solved for above is two dimensional makes it quite cumbersome to put it in the matrix form: we solve it by the method of conjugate residuals.

3. Numerical model for the generalized-Boussinesq equations

The departure point evaluation and the explicit solution of the depth equation proceed exactly as for the Green-Naghdi equations. Only the discretization of the momentum equation, Eq. (23), is different and is described below.

The gB momentum equations with the restoring terms included are

$$\frac{d\mathbf{u}}{dt} = -\nabla(\eta+b) + \frac{\eta_0}{2} D_t(\nabla\nabla\cdot(\eta_0\mathbf{u})) - \frac{\eta_0^2}{6} D_t(\nabla\nabla\cdot\mathbf{u}) - \frac{\mathbf{u}-\mathbf{u}_a}{\tau},$$

where D_t is the linear derivative $\partial_t+\mathbf{U}\cdot\nabla$, and where $\mathbf{U}$ is the constant ambient flow velocity. Approximating the above equation at the mid-point of the Lagrangian trajectory, we get

$$\frac{\mathbf{u}-\mathbf{u}_o}{\Delta t} = \frac{1}{2}(\nabla(b+\eta)+[\nabla(b+\eta)]_o) - \frac{1}{2}\left(\frac{\mathbf{u}-\mathbf{u}_a}{\tau} - \left[\frac{\mathbf{u}-\mathbf{u}_a}{\tau}\right]_o\right) - \frac{1}{2}\frac{\eta_0+[\eta_0]_{lo}}{2}\frac{\nabla\nabla\cdot(\eta_0\mathbf{u})-[\nabla\nabla\cdot(\eta_0\mathbf{u})]_{lo}}{\Delta t} - \frac{1}{6}\left(\frac{\eta_0+[\eta_0]_{lo}}{2}\right)^2\frac{\nabla\nabla\cdot\mathbf{u}-[\nabla\nabla\cdot\mathbf{u}]_{lo}}{\Delta t}, \tag{B15}$$

where Q_{lo} refers to the value of the quantity Q at the departure point corresponding to the uniform velocity $\mathbf{U}$ ($\mathbf{x}_{lo}=\mathbf{x}_i-\mathbf{U}$). Again as with the GN case, the above equation is linear in $\mathbf{u}$ and constitutes an elliptic problem which is solved by the method of conjugate residuals. Replacing Q_{l0} in the above discretization by Q_0, the value of Q evaluated at the nonlinear departure point resulted only in negligible changes to the solution.

The horizontal discretization, the time step, and the gravity wave absorbers are exactly the same as for the Euler model for both the GN and the gB models. The flow in the GN and gB models is started impulsively at time zero, and is unlike in the Euler model where the initial condition corresponds to the potential flow solution. The computation of the Euler solutions were carried out on the Cray YMP at National Center for Atmospheric Research and the computation of the SW and DSW solutions were carried out on the Connection Machine CM-5 in the Advanced Computing Lab at Los Alamos National Laboratory.

[1] R. Camassa, D. D. Holm, and C. D. Levermore, ''Long-time shallow water equations with a varying bottom,'' submitted to J. Fluid Mech.

[2] C. H. Su and C. S. Gardner, ''Korteweg-de Vries equation and generalizations. III. Derivation of the Korteweg-de Vries Equation and Burgers Equation,'' J. Math. Phys. **10**, 536 (1969).

[3] A. E. Green, N. Laws, and P. M. Naghdi, ''On the theory of water waves,'' Proc. R. Soc. London Ser. A **338**, 43 (1974).

[4] A. E. Green and P. M. Naghdi, ''A derivation of equations for wave propagation in water of variable depth,'' J. Fluid Mech. **78**, 237 (1976).

[5] J. W. Miles and R. Salmon, ''Weakly dispersive nonlinear gravity waves,'' J. Fluid Mech. **157**, 519 (1985).

[6] S. V. Bazdenkov, N. N. Morozov, and O. P. Pogutse, ''Dispersive effects in two-dimensional hydrodynamics,'' Sov. Phys. Dokl. **32**, 262 (1987).

[7] J. J. Shields and W. C. Webster, ''On direct methods in water-wave theory,'' J. Fluid Mech. **197**, 171 (1988).

[8] B. Wendroff, ''Composite flows,'' Physica D **60**, 208 (1992).

[9] Z. Demirbilek and W. C. Webster, ''Application of the Green-Naghdi theory of fluid sheets to shallow water wave problems,'' Technical Report of the Coastal Engineering Research Center-92-11, 1992.

[10] R. C. Ertekin, W. C. Webster, and J. V. Wehausen, ''Waves caused by a moving disturbance in a shallow channel of finite width,'' J. Fluid Mech. **169**, 275 (1986).

[11] G. B. Whitham, *Linear and Nonlinear Waves* (Wiley-Interscience, New York, 1944), p. 460.

[12] T. Y. Wu, ''Long waves in ocean and coastal waters,'' J. Eng. Mech. ASCE **107**, 501 (1981).

[13] R. Camassa and D. D. Holm, ''Dispersive barotropic equations for stratified mesoscale ocean dynamics,'' Physica D **60**, 1 (1992).

[14] D. M. Wu and T. Y. Wu, ''Three-dimensional nonlinear long waves due to moving surface pressure,'' *Proceedings of the 14th Symposium on Naval Hydrodynamics*, 1982, p. 103.

[15] S-J. Lee, G. T. Yates, and T. Y. Wu, ''Experiments and analyses of upstream-advancing solitary waves generated by moving disturbances,'' J. Fluid Mech. **199**, 569 (1989).

[16] J. G. Thews and L. Landweber, ''The influence of shallow water on the resistance of a cruiser model,'' U.S. Experimental Model Basin, Navy Yard, Washington, DC, Report No. 408, 1935.

[17] P. A. Madsen, R. Murray, and O. R. Sorensen, ''A new form of Boussinesq equations with improved linear dispersion characteristics,'' Coastal Eng. **15**, 371 (1991).

[18] O. Nwogu, ''An alternative form of the Boussinesq equations for near-shore wave propagation,'' J. Waterway Port Coast. Ocean Eng. **119**, 618 (1993).

[19] G. Wei, J. T. Kirby, S. T. Grilli, and R. Subramanya, ''A fully nonlinear Boussinesq model for surface waves. I. Highly nonlinear, unsteady waves,'' J. Fluid Mech. **294**, 71 (1995).

[20] D. D. Houghton and A. Kasahara, ''Nonlinear shallow fluid flow over an isolated ridge,'' Commun. Pure Appl. Math. **21**, 1 (1968).

[21] P. D. Lax, C. D. Levermore, and S. Venakides, ''The generation and propagation of oscillations in dispersive initial value problems and their limiting behavior,'' in *Important Developments in Soliton Theory*, edited by A. S. Fokas and V. E. Zakharov (Springer-Verlag, New York, 1993), p. 205.

[22] P. K. Smolarkiewicz and L. G. Margolin, ''On forward-in-time differencing for fluids: Eulerian and semi-Lagrangian nonhydrostatic models for stratified flows,'' Atmos. Ocean (in press).

[23] P. K. Smolarkiewicz and J. A. Pudykiewicz, ''A class of semi-Lagrangian approximations for fluids,'' J. Atmos. Sci. **49**, 2082 (1992).

[24] P. K. Smolarkiewicz and G. A. Grell, ''A class of monotone interpolation schemes,'' J. Comput. Phys. **101**, 431 (1992).

[25] B. T. Nadiga, ''An adaptive discrete-velocity model for the shallow water equations,'' J. Comput. Phys. **121**, 271 (1995).

[26] T. L. Clark, ''A small-scale dynamic model using a terrain-following coordinate transformation,'' J. Comput. Phys. **24**, 186 (1977).

[27] P. K. Smolarkiewicz and L. G. Margolin, ''Variational solver for elliptic problems in atmospheric flows,'' Appl. Math. Comput. Sci. **4**, 101 (1994).

[28] R. Rotunno and P. K. Smolarkiewicz, ''Vorticity generation in shallow-water equations as applied to hydraulic jumps,'' J. Atmos. Sci. **52**, 320 (1995).

[29] H. Lamb, *Hydrodynamics* (Dover, New York, 1945).

[30] C. Truesdell, *The Mechanical Foundations of Elasticity and Fluid Dynamics* (Gordon and Breach, New York, 1966), Chap. 3.22.